1 High spatial resolution analysis using indentation mapping differentiates biomechanical properties
2 of normal vs. degenerated mouse articular cartilage

3 Anand O. Masson[1,2], Bryce A. Besler[1,2], W. Brent Edwards[1,2,3], and Roman J Krawetz [1,2,4,5]*

4 [1] Biomedical Engineering Graduate Program, University of Calgary, Calgary, AB, Canada
5 [2] McCaig Institute for Bone and Joint Health, University of Calgary, Calgary, AB, Canada
6 [3] Human Performance Laboratory, Faculty of Kinesiology, University of Calgary, AB, Canada
7 [4] Department of Surgery, Cumming School of Medicine, University of Calgary, Calgary, AB Canada
8 [5] Department of Cell Biology and Anatomy, Cumming School of Medicine, University of Calgary,
9 Calgary, AB, Canada
10
11
12 *Corresponding Author Address: Dr. Roman J Krawetz, University of Calgary - 3330 Hospital Dr. NW.
13 Rm# HRIC 3AA10. Calgary, Alberta, Canada. T2N 4N1. Tel: (403)-210-6268. Email:
14 rkrawetz@ucalgary.ca

1

15 **Abstract**

16 Characterizing the biomechanical properties of articular cartilage is crucial to understanding processes

17 of tissue homeostasis vs. degeneration. In mouse models, however, limitations are imposed by their

18 small joint size and thin cartilage surfaces. Here we present a 3D automated surface mapping system

19 and methodology that allows for mechanical characterization of mouse cartilage with high spatial

20 resolution. We performed repeated indentation mappings, followed by cartilage thickness

21 measurement via needle probing, at 31 predefined positions distributed over the medial and lateral

22 femoral condyles of healthy mice. High-resolution 3D x-ray microscopy (XRM) imaging was used to

23 validate tissue thickness measurements. The automated indentation mapping was reproducible, and

24 needle probing yielded cartilage thicknesses comparable to XRM imaging. When comparing healthy

25 vs. degenerated cartilage, topographical variations in biomechanics were identified, with altered

26 thickness and stiffness (instantaneous modulus) across condyles and within anteroposterior sub-

27 regions. This quantitative technique comprehensively characterized cartilage function in mice femoral

28 condyle cartilage. Hence, it has the potential to improve our understanding of tissue structure-function

29 interplay in mouse models of repair and disease.

30

31

32

33

34

35

36

37

38

2

Introduction

The articular cartilage in synovial joints has a specialized three-dimensional structure and biochemical composition that provides low-friction, wear-resistance, and load-bearing properties to the tissue. Mechanical loading is essential to tissue homeostasis and influences gene expression, chondrocyte metabolism, extracellular matrix (ECM) maintenance, and associated interstitial fluid permeability [1,2]. Therefore, the biomechanical properties of cartilage are unique indicators of tissue homeostasis versus degeneration. Indeed, research into cartilage-related changes during the development of degenerative diseases such as osteoarthritis (OA) has demonstrated that early tissue dysfunction involves loss of proteoglycans and increased water content, resulting in reduced compressive strength and higher tissue permeability [3,4]. Disease progression leads to further structural damage and altered mechanics [5], ultimately resulting in tissue failure.

Mouse models are commonly used in pre-clinical studies focused on cartilage repair and pathophysiology of OA [6]. Mice are advantageous because of the well-established development of genetically modified strains [7] and the availability of diverse model systems mimicking mechanisms of spontaneous and induced tissue degeneration and regeneration [8–11]. In this regard, mouse models serve as powerful tools for the targeted assessment of cellular and molecular processes and the discovery of novel therapeutics related to cartilage regeneration and OA. Yet, while the structural integrity and biochemical composition of murine cartilage are routinely assessed through histological and molecular approaches, the evaluation of how these features translate into mechanical function is limited. The main challenge in mechanical function assessment stems from their small joint size and thin cartilage found in mice relative to other species [12]. Prior efforts to overcome these challenges include finite element modelling and optimization of small-scale indentation techniques [3,13–15].

Mechanical indentation (including AFM techniques), performed using either creep or stress-relaxation protocols, is widely employed for assessing the biomechanical behavior of cartilage and OA-related changes in many species [16–18], and considered the gold standard for small animal joints [19]. Unlike confined and unconfined compression tests, no sectioning or subsampling of tissue (i.e., cylindrical

3

67   explants) is required [20]. Instead, the cartilage tissue and its subchondral bone interface is kept intact,

68   providing more physiologically relevant data. Indentation is also advantageous in that it is non-

69   destructive and allows for repeated measures *in situ* [21]. However, the natural curvature of joint

70   articular surfaces poses a challenge to testing, as indentation must be conducted perpendicularly to the

71   surface [22].

72

73   Recently, a novel automated indentation technique has been developed for the mechanical assessment

74   of cartilage [23]. This commercially available multi-axial apparatus (Mach-1[TM], *Biomomentum Inc,*

75   Laval, QC) is capable of detecting specimen surface orientation at each position of measurement and

76   subsequently indent normal to the surface [23,24]. As such, it can map entire cartilage surfaces using a

77   single setup with high spatial density, and has been previously shown to discriminate between healthy

78   and diseased human cartilage samples [23,25]. This apparatus has been recently employed by Woods and

79   colleagues [26] to evaluate altered biomechanics in a mouse model of cartilage degeneration. However,

80   the study was conducted in the non-load-bearing region of the mouse knee joint. Considering that the

81   knee range of motion in mice is between 40° to 145° (i.e., unable to fully extend) [27], with normal gait

82   range between 90.5^o and 120° (extension-flexion) [28], the contact regions in the distal femoral condyles

83   are located further posteriorly compared to humans. Careful consideration of species-specific

84   differences in knee joint anatomy and kinematics is imperative for proper translation of pre-clinical

85   models [29].

86

87   Woods and colleagues [26] were also unable to account for site-specific cartilage thickness variations in

88   their measurements, instead using the mean cartilage thickness obtained via histological analysis in

89   their assessment [26]. Other studies have employed mean cartilage thickness values retrieved through

90   histology or imaging techniques to characterize and model tissue mechanical parameters in mice [13,15].

91   Implicit in this approach is the underlying assumption that cartilage thickness is relatively uniform

92   among medial and lateral compartments (e.g., femoral condyles or tibial plateaus) and along their

93   anteroposterior or mediolateral axis. Yet, regional variations in thickness are recognized within these

94   cartilage surfaces [12,15,30], and can impact indentation measurements [22,31].

95   Hence, the purpose of this study was to investigate the reliability of automated indentation mapping in

96   the assessment of healthy femoral articular cartilage in mice and characterize site-specific variations

97   in cartilage thickness. We also employed concurrent contrast-enhanced 3D x-ray microscopy (XRM)

98   imaging to validate the cartilage thickness measurements from our optimized needle probing protocol

99   [32]. Finally, this approach was used to investigate biomechanical differences in a clinically relevant

100   mouse model of cartilage degeneration [33]. Together, we show that automated indentation is reliable

101   and able to characterize topographic and mechanical variations across condyle cartilage locations in

102   intact cartilage. Moreover, this technique was able to identify regional changes in cartilage thickness

103   and stiffness in degenerated cartilage. A comprehensive and standardized biomechanical evaluation of

104   cartilage in repair and disease can greatly contribute to our understanding of tissue structure-function

105   interplay, thereby enhancing the clinical relevance of mouse models.

106

107   **Results**

108   *Automated indentation mapping reliability*

109   While previous studies have employed indentation mapping on mouse cartilage, to our knowledge

110   none have measured its accuracy and precision. Therefore, we performed three repeated mappings per

111   position for all specimens to undertake a reliability analysis of the automated surface indentation

112   technique. Each of the 31 predefined positions distributed over the femoral condyles of ten C57Bl6

113   mice was included in this analysis (Figure 1A). The setup was developed and optimized (Figure S1) to

114   assess the load-bearing regions of the femoral condyles and achieve non-destructive retrieval of

115   specimen post-testing for subsequent 3D XRM imaging analysis. The imposed step deformation (i.e.,

116   indentation depth) on the femoral cartilage yielded typical stress-relaxation behavior, characterized by

117   a sharp increase in force followed by gradual relaxation over time until equilibrium (Figure 1B).

118   Assessment of stress-relaxation and corresponding force-displacement curves (Figure 1B)

119   demonstrated consistency among repeated measurements for single positions and visible differences

120   in peak reaction forces between condyles. These observations were further evidenced by the spatial

121   distribution of peak force values across condylar testing sites (Figure 1C, Table S1). A total of 930

122   indentation measurements were retrieved, out of which only 21 produced invalid curves (seven testing

123   sites at specimen's periphery with higher angles yielded noisy signals, Figure 1C), representing a 2.26

124   % error rate during data acquisition. High reliability and absolute agreement between repeated

125   measures for individual testing sites were observed, with 4.7% intra-assay average coefficient of

126   variation (CV) (Table S1) and intraclass correlation coefficients - ICC (lower 95%, upper 95%) -

127   ranging from 0.974 (0.966, 0.981) for the lateral condyle to 0.971 (0.963, 0.978) for the medial

128   condyle. Mean peak force values illustrate site-specific variations within and between condyles

129   (Figure 1D). The lateral condyle values varied significantly per position ($p < 0.0001$), ranging from

130   0.07 to 0.15 N and showed a trend for higher values at outermost positions, with a slight decrease in

131   force posteriorly. The latter was also seen for the medial condyle, wherein heterogeneities in peak

132   force were also apparent ($p < 0.0001$) and had a wider range – from 0.15 to 0.294 N. Since the

133   analysis per testing site also reflects inherent deviations due to anatomical positioning across

6

134   specimens, data was pooled for regional (between condyles) and sub-regional (between and within

135   anteroposterior locations) comparisons.

136

137
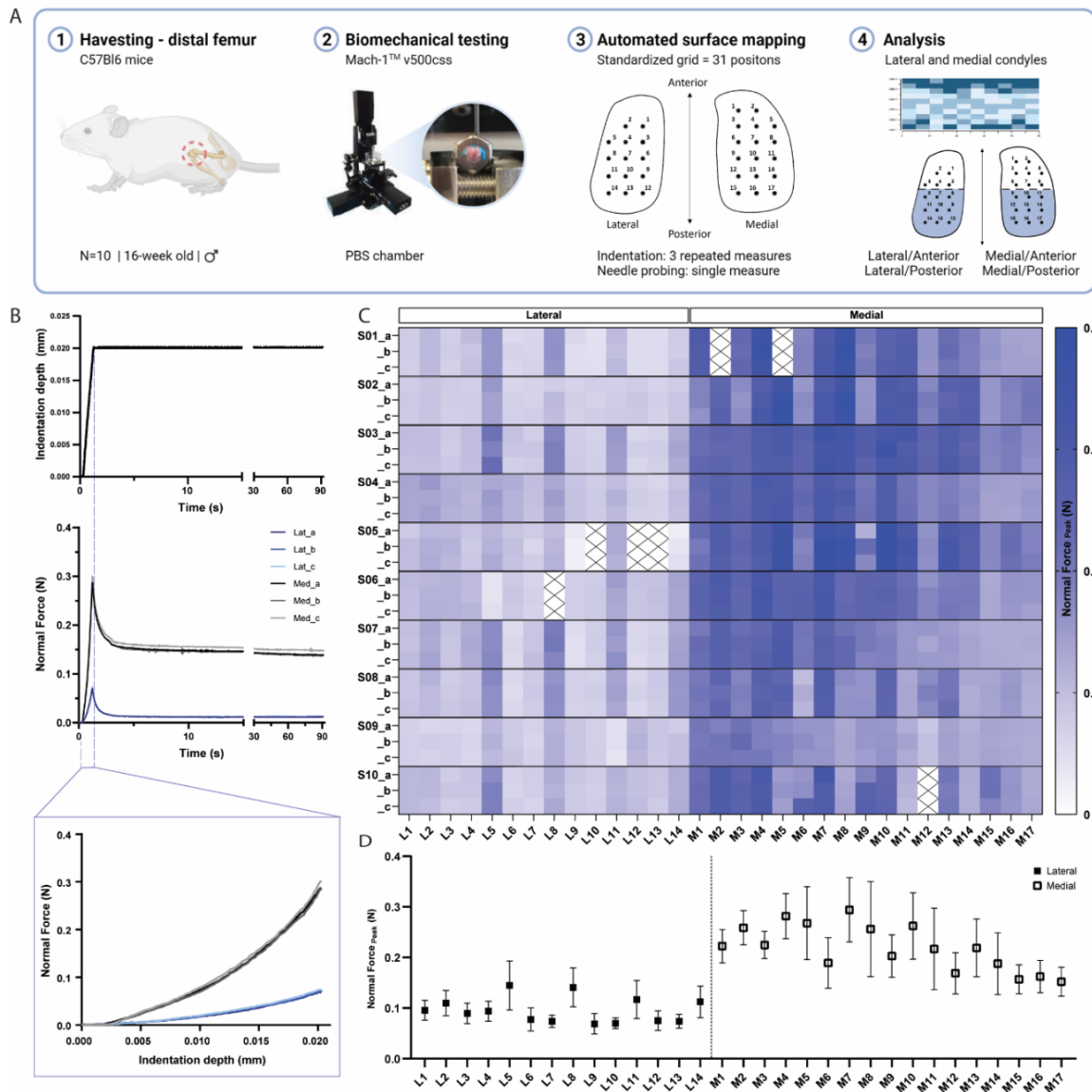
Figure 1. (A) Schematic overview of experimental design employed for biomechanical testing of murine articular cartilage using Mach-1^{TM} v500css mechanical tester (B) Step displacement used for cartilage indentation (top), with typical force-relaxation response curves obtained for three repeated measures on representative lateral and medial condyle positions (middle) and corresponding force increase with indentation depth (bottom) (C) Normal peak force recorded for all three repeated measures (a-c) considering each of the 31 testing sites, L1-L14 at lateral condyle and M1-M17 at medial condyle, for each specimen ($n = 10$, S01-S10), demonstrates general agreement for intra-specimen measurements on both condyles (D) Mean peak force values varied within and between condyle locations and higher within medial condyle testing sites. Data is presented as mean ± SD.

147

148

149

150

151

152 As Table 1 shows, the average peak force was significantly higher on the medial condyle and on both

153 its anterior and posterior sub-regions when compared to lateral counterparts (Lat/Ant vs. Med/Ant and

154 Lat/Post vs. Med/Post). Interestingly, no significant differences were observed between sub-regions of

155 the lateral condyle (Lat/Ant vs. Lat/Post). In contrast, the mean peak force yielded at the Med/Post

156 sub-region was 20% lower than on the Med/Ant ($p < 0.01$). As cartilage thickness variations between

157 and within condyle locations could affect peak forces measured at same indentation depth [34], with

158 thinner cartilage yielding higher force values, we sought to determine the cartilage thickness

159 distribution within the same surfaces and validate this approach using XRM imaging.

160

161 **Table 1.** Mean and standard deviation (SD) values for peak force (N) as determined by automated
162 indentation test performed for $n = 10$ distal femur samples of murine AC. Mean values compared
163 between condyles (Lateral/Medial; unpaired, Student's t test, $\alpha = 0.05$) and within sub-regions of
164 condyles (Lat/Ant, Lat/Post, Med/Ant, Med/Post; *one-way* ANOVA, $p < 0.05$).

Peak Force [N]				
Condyle	Mean (SD)	Condyle	Mean (SD)	Lat - Med
Lateral	0.096 (0.011)	Medial	0.219 (0.037)	*p < 0.0001*
Lat/Ant	0.107 (0.017)	*Med/Ant*	0.250 (0.037)	*p < 0.0001*
Lat/Post	0.090 (0.011)	*Med/Post*	0.199 (0.037)	*p < 0.0001*
Ant - Post	*ns*	Ant - Post	*p < 0.01*	-

165 *ns,* no significant difference; -, comparison not applicable

166
167

168 *Cartilage thickness characterization: comparison between needle probing and XRM imaging*

169 Needle probing (NP) thickness mapping was performed on all ten femoral condyles, which were

170 subsequently scanned using contrast enhanced XRM imaging. As shown in Figure 2A, reconstructed

171 3D datasets of murine distal femurs allowed us to validate the spatial distribution of NP testing sites,

172 thereby the corresponding ROI coordinates for imaging processing could be determined. Additionally,

173 the 2D slices confirmed that the needle probe pierced the full length of the cartilage, reaching the

174 subchondral bone (Figure 2A). The cartilage surface and cartilage-subchondral bone interface

175 positions were identified using the load-displacement curves from NP (Figure 2B) and the cartilage

176 thickness for each position was then calculated considering the surface angle (*Methods*). There was a

177   2.58% rate of needle probe failure (8 out of 310 measurements, testing sites near the specimen's edge)

178   during data acquisition. NP and contrast enhanced XRM imaging yielded similar cartilage thickness

179   distributions on both condyles (Figure 2C), demonstrating a highly significant correlation between

180   paired values (R = 0.842, n = 302, p < 0.0001) (Figure 2D). Further method-comparison using a

181   Bland-Altman plot (Figure 2E) illustrated XRM measurements were approximately 6.8 μm thicker on

182   average than needle probing, representing only a 1.55 voxels difference (4.39 μm resolution - XRM).

183   Moreover, no significant differences were found between pairwise mean thickness values (NP vs.

184   XRM) for individual positions within the lateral condyle (Figure 2F). Similar results were shown for

185   the medial condyle, wherein higher mean thickness values from XRM were only seen on M06 (Δ =

186   8.68 μm, p = 0.028), M11 (Δ = 9.89 μm, p < 0.01), and M13 (Δ = 9.34 μm, p = 0.012) testing sites.

187   No obvious reason for these localized differences were found, and dullness of needle was ruled out

188   since subsequent testing sites (M14 to M17) yielded comparable cartilage thickness values between

189   techniques.

190
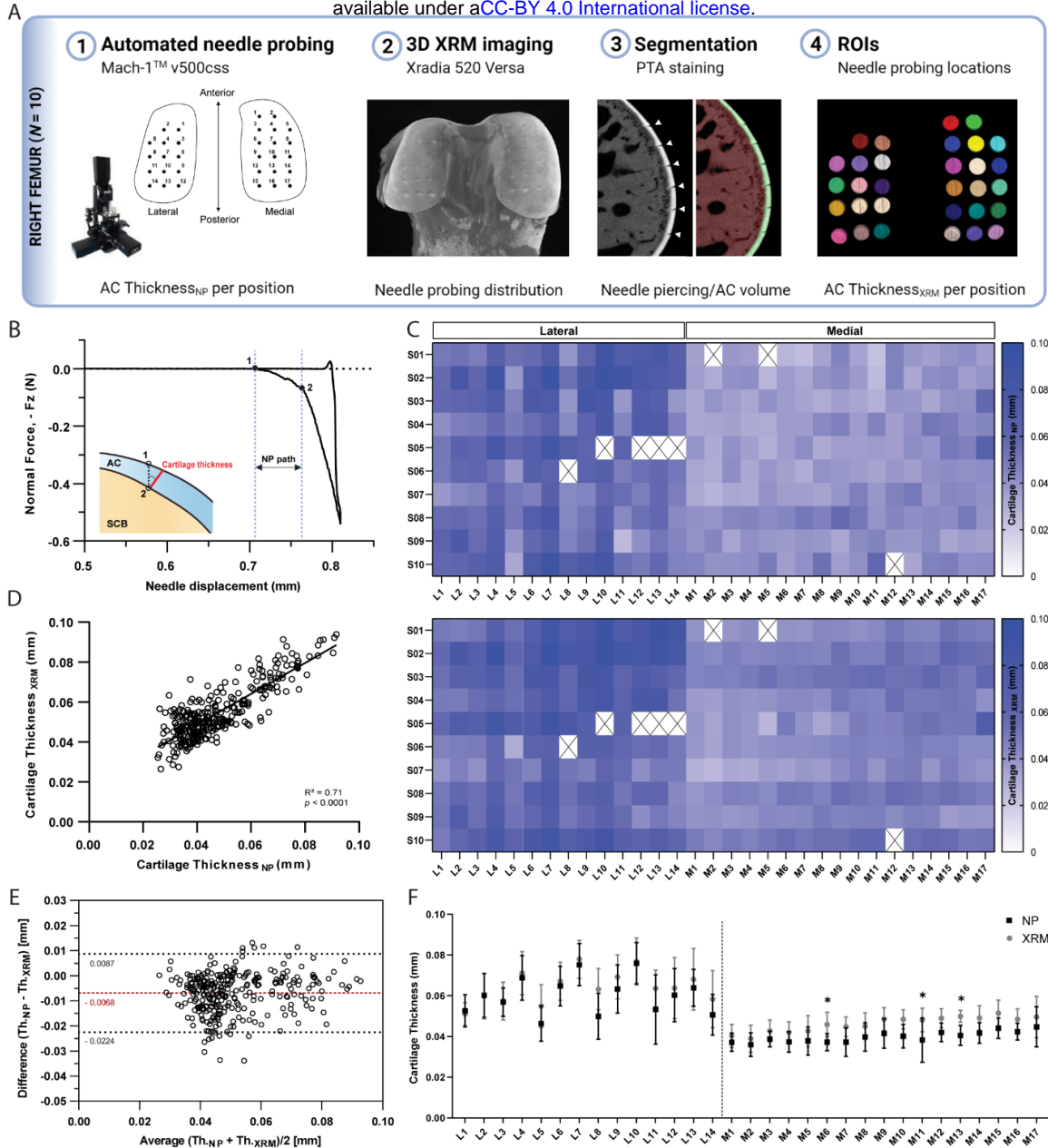
Figure 2. (A) Assessment of agreement between needle probing (NP) and XRM imaging cartilage thickness per position of measurement within right femoral condyles ($n = 10$) (B) Representative normal force-displacement curve obtained during NP test depicting articular cartilage, AC, surface (1) and subchondral bone, SCB, interface (2) positions and cartilage thickness calculated normal to the surface (*red*) using the surface angle orientation (C) Mapping distributions of cartilage thickness values per position as measured by NP and XRM (D) Correlation graph of cartilage thickness measured by NP vs. XRM, R = 0.842, n = 302, *p < 0.0001* and corresponding (E) Bland-Altman plot showing overall agreement between methods, with average difference of 6.8 µm in thickness. Dotted black lines show upper and lower 95% limit of agreement F) Pairwise assessment of mean cartilage thickness NP vs. XRM per position for the lateral and medial condyles (* *p < 0.05*, ** *p < 0.01*, *two-way* ANOVA). Symbols represent the means and error bars the standard deviation.

10

204 Unlike peak force distributions, spatial heterogeneities in cartilage thickness were apparent among

205 individual testing sites only on the lateral condyle ($p < 0.0001$), with averaged values ranging from 46

206 to 76 µm; whereas thickness distributions within the medial condyle was more uniform ($p = 0.06$),

207 ranging from 36 to 45 µm. Nevertheless, no significant differences were observed within condyles

208 when comparing their anteroposterior sub-regions; whereas the medial condyle was significantly

209 thinner than its lateral counterpart, both in its anterior and posterior sub-regions (Tables 2 and S2).

210 Together, cartilage thickness appears as a contributing factor but not the sole explanation to

211 mechanical variations, which is also affected by differences in composition and morphology.

212

213 **Table 2.** Mean and standard deviation (SD) values for cartilage thickness as determined by needle
214 probing for distal femur samples of murine articular cartilage ($n = 10$). Mean values compared
215 between condyles (Lateral/Medial; unpaired, Student's t test) and within sub-regions of condyles
216 (Lat/Ant, Lat/Post, Med/Ant, Med/Post; *one-way* ANOVA, $\alpha = 0.05$).

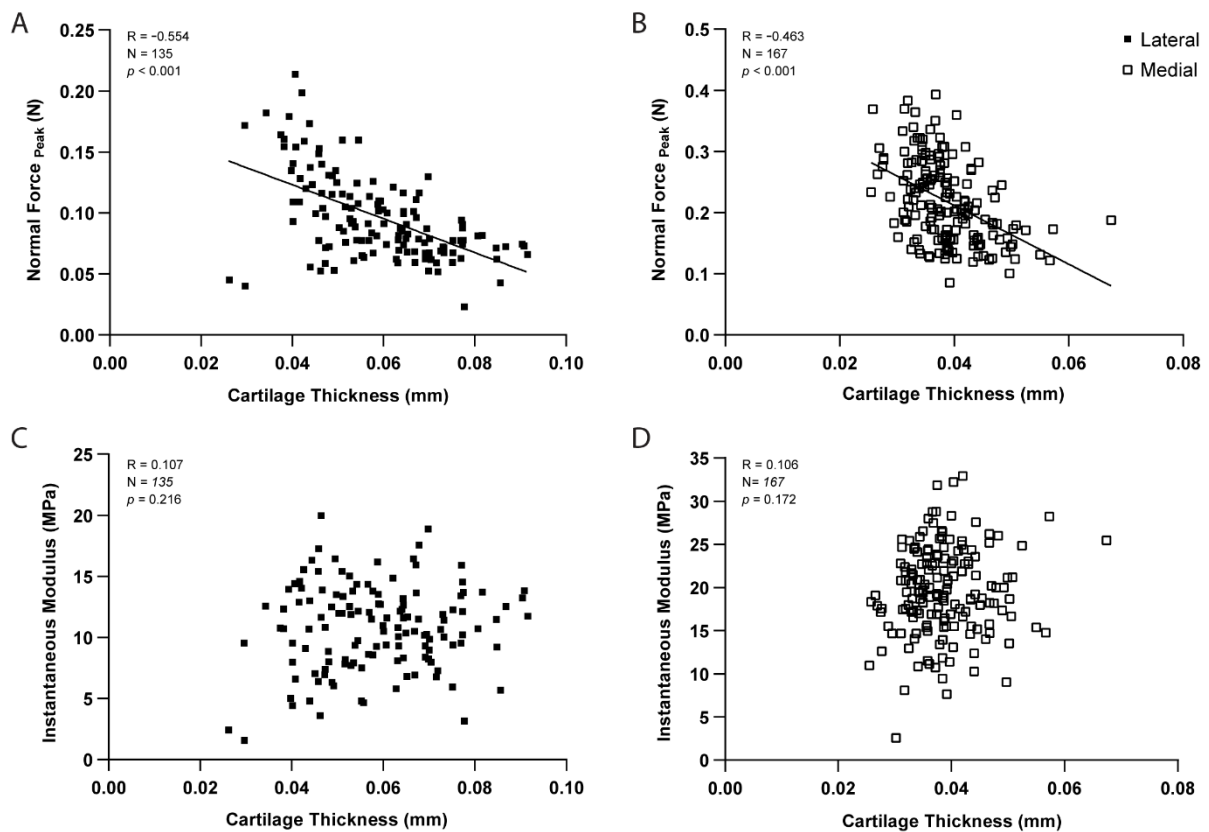| Cartilage Thickness [µm]				
Condyle	Mean (SD)	Condyle	Mean (SD)	Lat - Med
Lateral	60.3 (6.3)	Medial	39.8 (2.9)	$p < 0.0001$
Lat/Ant	57.0 (5.9)	*Med/Ant*	37.5 (3.8)	$p < 0.0001$
Lat/Post	62.3 (7.8)	*Med/Post*	41.9 (3.0)	$p < 0.0001$
Ant - Post	*ns*	Ant - Post	*ns*	-

217 *ns,* no significant difference; -, comparison not applicable

218

219

220 As expected, pairwise comparisons for individual testing sites demonstrated a significant negative

221 correlation between peak force and thickness measurements within lateral (R = −0.554, $n = 135$, $p <$

222 0.001, Figure 3A) and medial (R = −0.463, $n = 167$, $p < 0.001$, Figure 3B) condyles. Knowledge of

223 site-specific thickness variations allowed the compressive stiffness to be determined for the same

224 mechanical strain at each testing site. Instantaneous modulus was calculated using Hayes *et al.* elastic

225 model [31] at 20% strain, wherein linear elastic behavior can be assumed and instantaneous response is

226 considered as flow-independent (*Poisson's* ratio, $\upsilon = 0.5$ assumed) [35]. Regardless of femoral condyle,

227 instantaneous stiffness demonstrated no significant correlation to thickness variations (Figures 3C-D).

228 Notably, compressive stiffness differed significantly between condyles (Lat vs. Med, $p < 0.001$), but

229 no longer within a condyle (Lat/Ant vs Lat/Post: $p > 0.99$; Med/Ant vs Med/Post: $p = 0.546$), like

230 seen for peak reaction force on the medial side. Next, we assessed the potential of this indentation

231 testing in identifying microscale biomechanical differences between healthy and degraded cartilage.

232

233

234 **Figure 3.** Correlation graphs per testing site for the lateral (*n* = 135 positions) and medial (*n* = 167)
235 condyles, showing cartilage thickness (needle probing) is significantly correlated to peak indentation
236 force at 20 um (A-B), but not to instantaneous modulus values as determined by Hayes *et al.* (1972)
237 elastic model at 20% strain. *p*-values reported.

238
239
240

241 *Altered biomechanical properties in degenerated murine articular cartilage*

242 To assess the changes in mechanical response within the context of cartilage degeneration, we

243 employed the same testing protocol on age-matched Proteoglycan 4 (PRG4) knockout mice (*n* = 6)

244 and compared the outcomes to the C57Bl/6 controls. PRG4 is a mucin-like glycoprotein highly

245 conserved across species [36,37] and functionally relevant in joint homeostasis and lubrication [33,38,39].

246 PRG4 loss of function, as seen in knockout mice (*Prg4*^{-/-}), leads to degenerative joint changes

247 recapitulating the phenotype of human camptodactyly-arthropathy-coxavara-pericarditis (CACP)

248 syndrome [33,40]. Histological alterations of articular cartilage have been comprehensively described,

12

249   and include surface roughness, tissue thickening, and loss of collagen parallel orientation at the

250   superficial layer, progressing to irreversible tissue damage with age [33,41]. Yet, the microscale

251   assessment of site-specific mechanical variations, aside from friction, has not been described so far

252   for $Prg4^{-/-}$ knee cartilage surfaces. Mapping of biomechanical parameters allowed site-specific

253   differences in $Prg4^{-/-}$ cartilage to be visualized, and outcomes were largely reproducible across

254   femoral specimens (Figure 4A-B). These findings were supported by the combined quantitative

255   assessment between genotypes for the different condyle regions and subregions (Figure 4C-F). $Prg4^{-/-}$

256   mean cartilage thickness on both lateral (67.9 ± 3.5 μm, $p = 0.032$) and medial (56.3 ± 3.7 μm, $p <$

257   0.001) sides of the knee was higher compared to controls (Figure 4C). Differences in cartilage

258   thickness between genotypes on anteroposterior sub-regions, however, were only detected on the

259   medial condyle (Figure 4E). The site-specific thickness measurements enabled us to determine the

260   instantaneous modulus at each testing site for the same mechanical strain. The utilized Hayes *et al.*

261   elastic model could fit the response of mouse cartilage with great accuracy (RMSE equal to 0.017 ±

262   0.007 MPa for controls and 0.010 ± 0.003 MPa for $Prg4^{-/-}$). Cartilage compressive stiffness was

263   significantly lower on the medial condyle of $Prg4^{-/-}$ mice compared to controls (8.67 ± 1.79 MPa vs.

264   19.52 ± 2.44 MPa, respectively, $p < 0.001$). Similar patterns were seen when considering the

265   anteroposterior subregions of the medial condyle (Figures 4F). No significant differences in lateral

266   condyle cartilage stiffness were observed (10.85 ± 1.73 MPa - control vs. 8.73 ± 2.39 MPa - $Prg4^{-/-}$, p

267   $= 0.187$).

13
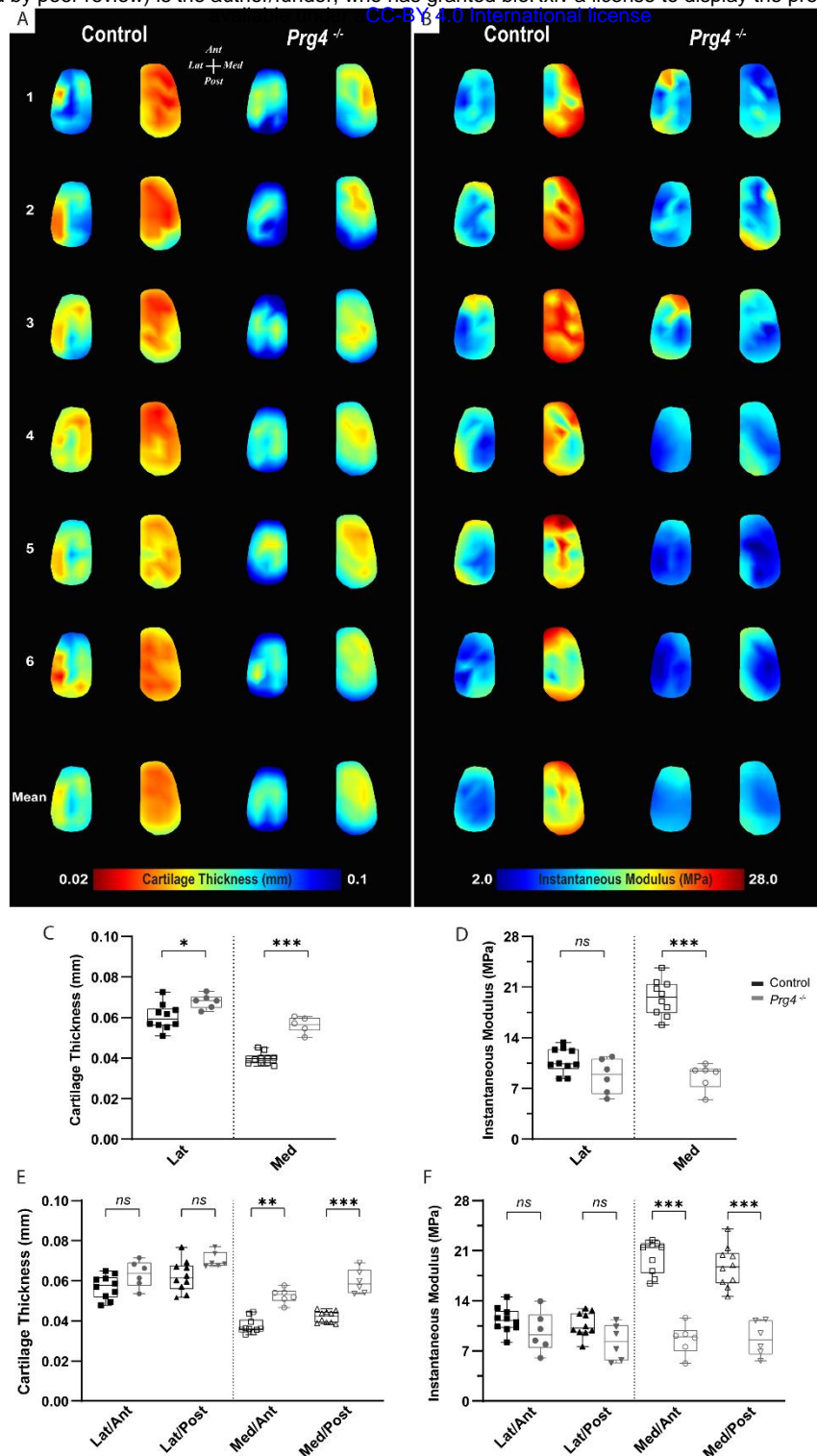
Figure 3. (A-B) Heat maps and corresponding boxplots comparing (C-D) regions - lateral and medial - and their (E-F) sub-regions - Lat/Ant, Lat/Post, Med/Ant, Med/Post - highlight spatial differences in biomechanical parameters on femoral cartilage surface between controls (C57Bl/6, $n = 10$) and PRG4 knockout mice ($Prg4^{-/-}$, $n = 6$). Maps shown for six representative samples per genotype, as well as the corresponding averaged map of all samples. Parameters illustrated are thickness measured by NP (A, C, E) and instantaneous modulus as determined by Hayes *et al.* (1972) elastic model (B, D, F). Pairwise comparison between genotypes for mean values on the lateral and medial condyles and

14

276   anteroposterior sub-regions (*Mann-Whitney U* with *Bonferroni-Dunn* correction, $^{*}p < 0.05$, $^{**}p < 0.01$,

277    $^{***}p < 0.001$).

Discussion

279   Using a novel microscale instrumented apparatus, we were able to reliably detect and quantify spatial

280   variations in biomechanical parameters across murine cartilage surfaces, both within healthy and

281   degenerated femoral condyles. Compared to recent mouse studies using this commercially available

282   apparatus [26,42], the optimization of sample mounting and needle probing protocols allowed for

283   unprecedented quantitative mapping of the mechanical behavior and associated cartilage thickness on

284   load-bearing regions of distal femurs with high spatial density.

285

286   For healthy, 4-month old C57Bl6 mice, micro-indentation measurements were reproducible at any

287   given testing site, also indicating that the instantaneous deformation employed and subsequently

288   sustained compression protocol did not compromise the mechanical behavior of the freshly harvested

289   cartilage tissue. In addition, heterogeneity in peak forces were identified across anatomical locations.

290   Notably, the medial condyle surface yielded approximately two times higher peak forces on average

291   than its lateral counterpart. Moreover, both condyles displayed a shift towards lower values at

292   posterior regions. Previous studies have shown significant variation in mechanical properties within

293   different cartilage surfaces in healthy joints [43,44], or even over a single surface [18,45]. However, the

294   effect of site-specific cartilage geometry, such as thickness, when characterizing the mechanical

295   properties of cartilage in indentation is often overlooked [23,46].

296

297   Studies in mice commonly rely on mean thickness values from histology, requiring longer turnaround

298   and lacking spatial specificity. The optimized needle probing protocol used here, was able to resolve

299   spatial thickness variations across condyle surfaces, and for the first-time closely localize cartilage

300   thickness measures to the footprint of indentation on mouse distal femurs. Moreover, three-

301   dimensional visualization of the femoral cartilage surfaces after XRM imaging validated the

302   positioning and distribution of the testing grid used, allowed us to pinpoint individual testing sites and

303   compute their thickness. A highly significant correlation between pairwise cartilage thickness values

304   from NP and XRM, per measurement site, was observed. Small variations seen between averaged

305   thickness values could be explained by differences in instrument resolution capabilities (Mach-1 z-

306   axis: 0.5 µm vs XRM: 4.39 µm voxel size), partial volume effects in XRM segmentation, and/or

307   compromise of cartilage integrity by needle probing, which might have led to cartilage swelling and

308   overestimation on subsequent XRM thickness measures. Nevertheless, mean thickness values were in

309   line with earlier reports for mouse cartilage [29,47,48], and marked greater cartilage thicknesses were

310   measured on the lateral condyle compared to the medial counterpart [12].

311

312   In general, higher peak reaction forces in intact cartilage were associated with lower thickness values

313   at the same indentation depth, and likely amplified by contribution of the underlying subchondral

314   bone on thinner areas [49]. Localized cartilage thickness measurements enabled us to account for the

315   effect of cartilage geometry when calculating compressive stiffness distributions. Quantitative

316   analysis was adjusted to 20% strain (considered as physiological loading) [50], and corresponding

317   instantaneous modulus could be derived from Hayes's analytical formulation. According to the

318   present results, there was no significant variation in mean thickness of healthy cartilage over a

319   condyle surface, therefore biomechanical parameters were compared between matched regions and

320   sub-regions when assessing degeneration.

321

322   Compared to C57Bl6 control, the loss of *Prg4* function resulted in an increase in thickness and

323   decrease in stiffness of the knee cartilage in 16-weeks-old mice. This is consistent with previous

324   observations on hip articular cartilage of *Prg4*^{-/-} mice (same age), using nanoscale atomic force

325   microscopy (AFM) indentation [39]. The cartilage thickness values determined by needle probing in our

326   study are in a similar range to those reported by Karamchedu *et al.* [41]. In their microCT imaging

327   study, *Prg4*^{-/-} mice displayed cartilage thickness averaging 61.0 ± 4.3 µm and 42.4 ± 2.6 µm for the

328   load-bearing regions of the lateral and medial condyle, respectively. Furthermore, *Prg4*^{-/-} cartilage

329   was significantly thicker than in control littermates, even though mice were younger (10-weeks-old)

330   than in our study.

331

332   Reduction in the instantaneous compressive modulus in our study was confined to the medial

333   compartment. We attribute that to differences in thickening in *Prg4*^{-/-} femoral cartilage compared to

334   controls, 12.6% versus 41% on lateral and medial condyles respectively, as well as *Prg4*^{-/-}

335   compromised structural integrity [33,38,51] having a bigger functional impact on the medial compartment,

336   recognized as the main load bearing region in most mammalian joints. Microscale indentation

337   characterizes the overall tissue resistance to deformation [50]. Due to the rapid compression rate

338   employed in the present protocol, normal cartilage tissue is expected to deform with minimal change

339   in volume [35], as its low permeability restrains fluid flow; thereby localizing the strain near the surface

340   as fluid pressure pushes against the collagen meshwork. Thus, under instantaneous (impact) loading

341   the ability of cartilage to resist compression is known to be affected by the collagen fibril meshwork

342   [49,52], particularly tangentially oriented collagen fibrils on the superficial tissue layer [43]. In *Prg4*^{-/-} the

343   normal parallel organization of collagen fibrils adjacent to the surface is known to be disrupted [38],

344   likely affecting tissue permeability as well, helping explain the lower instantaneous modulus and

345   slightly faster dissipation of stress.

346

347   Limitations of this study include evaluation of the anatomy of the distal murine femoral condyles and

348   not the opposing articulation (i.e., proximal tibia). Also, we focused on a single timepoint analysis,

349   however, investigations related to aging and progressive degeneration are of interest, as they are

350   known to affect the biochemical composition and structural integrity of cartilage [33,53,54], thereby

351   influencing its mechanical properties. Finally, due to the biphasic/poroviscoelastic nature of cartilage,

352   future studies could consider the use of more complex analytical models [55,56] able to capture the

353   viscoelastic behavior of cartilage in mice.

354

355   In this study, we have gained insights into the patterns of varying surface geometry, and mechanics

356   present within murine articular cartilage at the microscale. Three-dimensional indentation mapping

357   was able to resolve site-specific differences in thickness and mechanical properties across knee

358   cartilage surfaces in healthy mice. Moreover, it identified functional changes on the *Prg4*^{-/-} mouse

359   model. This technique could also prove helpful for the study of other mouse models mimicking

360   different mechanisms of, or therapies focused on, repair and degeneration of articular cartilage, as

361   microscale indentation with high spatial density can provide a more comprehensive characterization

362   of cartilage's mechanical properties.

363

364   **Materials and methods**

365   *Ethics statement*

366   All mouse experiments were carried out following the Canadian Council on Animal Care Guidelines

367   recommendations and approved by the University of Calgary Animal Care Committee (protocols

368   AC16-0043 and AC20-0042).

369   *Animals*

370   Male C57Bl6 mice were purchased from *Jackson Laboratories* (Bar Harbor, ME). We based on

371   sample on a recent paper that used indentation (but not needle probing) in mice [26], however, because

372   of the addition of needle probing we decided to increase the sample size. Animals were housed under

373   a standard light cycle and had free access to feed (standard diet) and water. Ten mice were euthanized

374   at 16-weeks of age, and hind limbs ($n = 10$ right) were harvested for biomechanical testing and 3D X-

375   ray microscopy (XRM) imaging. Age-matched PRG4 knockout mice ($Prg4^{-/-}$, $n = 6$) were generated

376   and maintained on a C57BL/6 genetic background, as previously described [57]. Limbs were

377   disarticulated at the hip, followed by transection of the ligaments and careful isolation of distal femurs

378   from tibiae and menisci with the help of a dissection microscope (*Leica*). Femurs were preserved

379   gently wrapped in Kimwipe soaked in phosphate-buffered saline (PBS, pH 7.4) until the time of

380   assessment. All samples were mechanically tested no longer than 3h after dissection to prevent tissue

381   degradation.

382   *Automated Indentation Mapping*

383   The shafts of isolated femurs were glued into a 0.1-10 µL pipette tip (*VWR*) using cyanoacrylate

384   adhesive, fixed into a stainless-steel hex nut (*Paulin*, Model 848-216) and secured to the sample

385   holder (Figure S1). This customized setup allowed for simple and proper positioning of the sample

386   exposing the load-bearing region of the condyles [27] for data acquisition, as well as non-destructive

387   retrieval of samples after testing, such that subsequent XRM imaging could be carried out. A

388   standardized mapping grid ($n = 31$ positions) was superimposed on an image of the cartilage surface,

389   consisting of 14 and 17 measurement sites at the lateral and medial condyles, respectively (Figure

390   1A). The testing chamber was filled with PBS solution at room temperature, and the tissue was

391   allowed to equilibrate before testing. Automated indentation mapping under stress-relaxation was then

392   performed using the Mach-1TM v500css (Biomomentum Inc., Laval, QC) device, equipped with a

393   calibrated multiple-axis load cell (±17 N, 3.5 mN force resolution) and associated software. With each

394   site, the contact coordinates (and contact coordinates at four adjacent places in a 0.075 mm scanning

395   grid) were measured using a contact criteria of 0.035 N. Surface orientation was then calculated using

396   the surrounding contact coordinates. Indentation was achieved by moving the indenter perpendicular

397   to the surface while moving the Mach-1 stages concurrently in all 3-axis. The spherical indenter (0.3

398   mm in diameter) was driven into the cartilage to a depth of 20 μm over one second and held constant

399   for 90 seconds. For C57Bl6, a total of 3 indentation tests were performed per sample, approximately

400   45 minutes apart. Data reported consist of peak force and instantaneous modulus, as determined by

401   fitting the Hayes et al. (1972) [31] elastic model to the load-displacement curves at 20% strain.

402   Assessment of how well the model fit the resulting curve per test site was done using root mean

403   square error (RSME). Since the analysis per position across specimens and genotypes reflect

404   deviations due to anatomical positioning, calculated parameters were compared between lateral (Lat)

405   and medial (Med) femoral condyles, as well as on four condylar sub-regions (Lateral/Anterior -

406   Lat/Ant, Lateral/Posterior – Lat/Post, Medial/Anterior - Med/Ant, Medial/Posterior - Med/Post), each

407   containing at least 5 positions of measurement (Figure 1A).

408   *Needle probing – thickness measurement*

409   After indentation mapping, the spherical indenter was replaced by a 30G x 1.4" hypodermic needle

410   (TSK Laboratory, Japan) adapted to the 1 mm spherical indenter (*Biomomentum Inc.*, Laval, Canada)

411   (Figure S2). Automated thickness mapping (Figure 2A) was done on the knee cartilage surface using

412   the needle probing technique [32], and previous mapping grid distribution slightly shifted as appropriate

413   to account for the off-axis position of the needle's bevel tip. The needle was driven vertically into the

414   cartilage surface at a constant speed until a 0.5 N stop criteria was reached in the subchondral bone.

415   The cartilage surface and cartilage/subchondral bone interface positions were identified in the load-

416   displacement curves (Figure 2B) generated at each measurement site using the automatic mode of

417   analysis [24]. A 0.25 N/s loading limit was defined to identify the interface position. Manual correction

418   was employed when the algorithm failed to identify the inflection point [24]. The cartilage thickness

419   reported corresponds to the vertical needle displacement from cartilage surface to subchondral bone

420   multiplied by the cosine of the surface orientation angle (Figure 2B) as determined during automated

421   indentation for each position. After testing, samples were preserved in 10% NBF solution for 24h and

422   stored in 70% ethanol for 24h to 48h before imaging.

423   *3D X-ray Microscopy (XRM) imaging*

424   3D XRM imaging was used for non-destructive assessment of cartilage morphology after

425   biomechanical testing. Fixed femurs were incubated for 16-18h in 1% phosphotungstic acid (PTA)

426   solution at room temperature for cartilage contrast enhancement before imaging [15]. Samples were

427   enclosed onto a custom specimen chamber, with 1% PTA in 70% ethanol added to the chamber's

428   bottom to minimize tissue dehydration. Zeiss Xradia 520 versa (*Carl Zeiss* X-Ray Microscopy,

429   Pleasanton, CA) scans of each distal femur were obtained following previously described protocol

430   [58,59]. In brief, high-resolution scans of 2001 axial slices were acquired at a 4.39 μm voxel size, with

431   low-energy (40 kVp voltage, 3 W power) x-rays.

432   *Imaging processing*

433   The contrast-enhanced cartilage surface was segmented by determining a threshold intensity, thereby

434   delineating the femur scan into cartilage and subchondral bone voxels. Needle probing left a physical

435   deformity in the articular cartilage of the right femurs visible on XRM imaging (Figure 2A), allowing

436   for all 31 regions of interest (ROIs) corresponding to needle probing to be manually landmarked.

437   Landmarks were placed manually using the two-dimensional axial, sagittal, and coronal planes

438   centered along the cartilage thickness and within each needle probing site. Cartilage segmentations

439   were corrected manually to ensure the cartilage mask encompassed resulting volume gaps at needle

440   probing positions. Then, the segmented cartilage was masked by a sphere of radius 75 μm placed on

441   each landmark, leaving a thin disk of cartilage. The thickness transform was computed for each disk [60]

442   and the mean thickness values, taken as a statistic of the thickness distribution, were used to minimize

443   variability due to morphological changes in the cartilage caused by the mechanical testing. Image

444   processing was performed in SimpleITK [61] (Insight Software Consortium, v1.2.4), and morphometry

445   was performed in Image Processing Language (IPL v5.42, SCANCO Medical AG, Brüttisellen,

446   Switzerland).

447   *Statistical analysis*

448   Analyses were performed in GraphPad Prism software (version 9), $\alpha = 0.05$ was considered statically

449   significant. Continuous parameters are reported as mean values and corresponding standard deviations

450   (SDs). Normality was assessed by Shapiro-Wilk normality test. C57Bl6 peak load and thickness data

451   was analysed by Student *t* test or ANOVA, with Bonferroni *post-hoc* comparisons. To assess

452   differences in biomechanical properties between genotypes non-parametric Mann-Whitney U test

453   with *Bonferroni-Dunn's* correction was used. To test reliability and absolute agreement between

454   repeated measurements, SPSS 27 (*IBM*, Chicago, IL) was used to obtain single-measurement, two-

455   way mixed effect intraclass correlation coefficient estimates and respective 95% limits of agreement

456   [62,63]. When assessing cartilage thickness measurements between needle probing and XRM imaging

457   techniques, *Pearson* correlation coefficient (R) was used for method-comparison and Bland-Altman

458   analysis to assess bias between methods.

459

460

461

462

463

464

465

466

467

468

469

470

471

472

473

474

475

476 **Acknowledgments**

481

482 **Author's contribution**

483 A.O.M. was responsible for the study design, data collection, data analysis, data interpretation and

484 draft of the manuscript. B.B. carried out imaging processing and data analysis. W.B.E. contributed to

485 the study design. R.K. contributed to the study design and data interpretation. B.B., W.B.E. and R.K.

486 provided critical review, commentary and revisions to the manuscript.

487

488   **References**

489   1.   Vincent, T. L. & Wann, A. K. T. Mechanoadaptation: articular cartilage through thick and

490   thin. *J. Physiol.* **597**, 1271–1281 (2019).

491   2.   Grodzinsky, A. J., Levenston, M. E., Jin, M. & Frank, E. H. Cartilage Tissue Remodeling in

492   Response to Mechanical Forces. *Annu. Rev. Biomed. Eng.* **2**, 691–713 (2000).

493   3.   Stolz, M. *et al.* Early detection of aging cartilage and osteoarthritis in mice and patient samples

494   using atomic force microscopy. *Nat. Nanotechnol.* **4**, 186–192 (2009).

495   4.   Setton, L. A., Mow, V. C., Müller, F. J., Pita, J. C. & Howell, D. S. Mechanical Properties of

496   Canine Articular Cartilage Are Significantly Altered Following Transection of the Anterior

497   Cruciate Ligament. *J. Orthop. Res.* **12**, 451–463 (1994).

498   5.   Kleeman, R. U., Krocker, D., Cedrano, A., Tuischer, J. & Duda, G. N. Altered cartilage

499   mechanics and histology in knee osteoarthritis: Relation to clinical assessment (ICRS Grade).

500   *Osteoarthr. Cartil.* **13**, 958–963 (2005).

501   6.   McCoy, A. M. Animal Models of Osteoarthritis. *Vet. Pathol.* **52**, 803–818 (2015).

502   7.   Helminen, H. J., Säämänen, A. M., Salminen, H. & Hyttinen, M. M. Transgenic mouse models

503   for studying the role of cartilage macromolecules in osteoarthritis. *Rheumatology* **41**, 848–856

504   (2002).

505   8.   Bedelbaeva, K. *et al.* Lack of p21 expression links cell cycle control and appendage

506   regeneration in mice. *Proc. Natl. Acad. Sci. U. S. A.* **107**, 5845–50 (2010).

507   9.   Kyostio-Moore, S. *et al.* STR/ort mice, a model for spontaneous osteoarthritis, exhibit elevated

508   levels of both local and systemic inflammatory markers. *Comp. Med.* **61**, 346–355 (2011).

509   10.   Murphy, M. P. *et al.* Articular cartilage regeneration by activated skeletal stem cells. *Nat. Med.*

510   **26**, 1583–1592 (2020).

511   11.   Christiansen, B. A. *et al.* Non-invasive mouse models of post-traumatic osteoarthritis.

512   *Osteoarthr. Cartil.* **23**, 1627–1638 (2015).

513   12.   Malda, J. *et al.* Of Mice, Men and Elephants: The Relation between Articular Cartilage

514   Thickness and Body Mass. *PLoS One* **8**, 1–8 (2013).

515   13.   Cao, L., Youn, I., Guilak, F. & Setton, L. A. Compressive properties of mouse articular

516   cartilage determined in a novel micro-indentation test method and biphasic finite element

517   model. *J. Biomech. Eng.* **128**, 766–771 (2006).

518   14.   Berteau, J. P., Oyen, M. & Shefelbine, S. J. Permeability and shear modulus of articular

519   cartilage in growing mice. *Biomech. Model. Mechanobiol.* **15**, 205–212 (2016).

520   15.   Das Neves Borges, P., Forte, A. E., Vincent, T. L., Dini, D. & Marenzana, M. Rapid,

521   automated imaging of mouse articular cartilage by microCT for early detection of

522   osteoarthritis and finite element modelling of joint mechanics. *Osteoarthr. Cartil.* **22**, 1419–

523   1428 (2014).

524   16.   Athanasiou, K. A., Rosenwasser, M. P., Buckwalter, J. A., Malinin, T. I. & Mow, V. C.

525   Interspecies comparisons of in situ intrinsic mechanical properties of distal femoral cartilage.

526   *J. Orthop. Res.* **9**, 330–340 (1991).

527   17.   Risch, M. *et al.* Mechanical, biochemical, and morphological topography of ovine knee

528   cartilage. *J. Orthop. Res.* **39**, 780–787 (2021).

529   18.   Hoch, D. H., Grodzinsky, A. J., Koob, T. J., Albert, M. L. & Eyre, D. R. Early changes in

530   material properties of rabbit articular cartilage after meniscectomy. *J. Orthop. Res.* **1**, 4–12

531   (1983).

532   19.   Lakin, B. A., Snyder, B. D. & Grinstaff, M. W. Assessing Cartilage Biomechanical Properties:

533   Techniques for Evaluating the Functional Performance of Cartilage in Health and Disease.

534   *Annu. Rev. Biomed. Eng.* **19**, 27–55 (2017).

535   20.   Mansour, J. M. Biomechanics of cartilage. *Kinesiol. Mech. Pathomechanics Hum. Mov.*

536   *Second Ed.* 69–83 (2013).

537   21.   Lu, X. L. & Mow, V. C. Biomechanics of Articular Cartilage and Determination of Material

538   Properties. *Med. Sci. Sport. Exerc.* **40**, 193–199 (2008).

539   22.   Swann, A. C. & Seedhom, B. B. Improved Techniques for Measuring the Indentation and

540   Thickness of Articular Cartilage. *Proc. Inst. Mech. Eng. Part H J. Eng. Med.* **203**, 143–150

541   (1989).

542   23.   Sim, S. *et al.* Electromechanical Probe and Automated Indentation Maps Are Sensitive

543   Techniques in Assessing Early Degenerated Human Articular Cartilage. *J. Orthop. Res.* 858–

544   867 (2017) doi:10.1002/jor.23330.

545   24.   Biomomentum. *Mach-1 Analysis User Manual v6.4*. (2020).

546   25.   Seidenstuecker, M. *et al.* Viscoelasticity and histology of the human cartilage in healthy and

547   degenerated conditions of the knee. *J. Orthop. Surg. Res.* **14**, 256 (2019).

548   26.   Woods, P. S. *et al.* Automated Indentation Demonstrates Structural Stiffness of Femoral

549   Articular Cartilage and Temporomandibular Joint Mandibular Condylar Cartilage Is Altered in

550   FgF2KO Mice. *Cartilage* 194760352096256 (2020) doi:10.1177/1947603520962565.

551   27.   Jia, H. *et al.* Loading-Induced Reduction in Sclerostin as a Mechanism of Subchondral Bone

552   Plate Sclerosis in Mouse Knee Joints During Late-Stage Osteoarthritis. **70**, 230–241 (2018).

553   28.   Hu, X., Charles, J. P., Akay, T., Hutchinson, J. R. & Blemker, S. S. Are mice good models for

554   human neuromuscular disease? Comparing muscle excursions in walking between mice and

555   humans. *Skelet. Muscle* **7**, 1–15 (2017).

556   29.   Oláh, T., Michaelis, J. C., Cai, X., Cucchiarini, M. & Madry, H. Comparative anatomy and

557   morphology of the knee in translational models for articular cartilage disorders. Part II: Small

558   animals. *Ann. Anat. - Anat. Anzeiger* **234**, (2021).

559   30.   Li, G. *et al.* The cartilage thickness distribution in the tibiofemoral joint and its correlation

560   with cartilage-to-cartilage contact. *Clin. Biomech.* **20**, 736–744 (2005).

561   31.   Hayes, W. C., Keer, L. M., Herrmann, G. & Mockros, L. F. A mathematical analysis for

562   indentation of articular cartilage. *J. Biomech.* **5**, 541–551 (1972).

563   32.   Jurvelin, J. S., Räsänen, T., Kolmonens, P. & Lyyra, T. Comparison of optical, needle probe

564   and ultrasonic techniques for the measurement of articular cartilage thickness. *J. Biomech.* **28**,

565   231–235 (1995).

566   33.   Rhee, D. K. *et al.* The secreted glycoprotein lubricin protects cartilage surfaces and inhibits

567   synovial cell overgrowth. *J. Clin. Invest.* **115**, 622–31 (2005).

568   34.   Michalak, G. J., Walker, R. & Boyd, S. K. Concurrent Assessment of Cartilage Morphology

569   and Bone Microarchitecture in the Human Knee Using Contrast-Enhanced HR-pQCT

570   Imaging. *J. Clin. Densitom.* **22**, 74–85 (2019).

571   35.   Armstrong, C. G. An analysis of the stresses in a thin layer of articular cartilage in a synovial

572   joint. *Eng. Med.* 55–61 (1986).

573   36.   Askary, A. *et al.* Ancient origin of lubricated joints in bony vertebrates. *Elife* **5**, 1–13 (2016).

574   37.   Ikegawa, S., Sano, M., Koshizuka, Y. & Nakamura, Y. Isolation, characterization and mapping

575   of the mouse and human PRG4 (proteoglycan 4) genes. *Cytogenet. Cell Genet.* **90**, 291–7

576   (2000).

577   38.   Jay, G. D. *et al.* Association between friction and wear in diarthrodial joints lacking lubricin.

578   *Arthritis Rheum.* **56**, 3662–3669 (2007).

579   39.   Coles, J. M. *et al.* Loss of cartilage structure, stiffness, and frictional properties in mice lacking

580   PRG4. *Arthritis Rheum.* **62**, 1666–1674 (2010).

581   40.   Marcelino, J. *et al.* CACP, encoding a secreted proteoglycan, is mutated in camptodactyly-

582   arthropathy-coxa vara-pericarditis syndrome. *Nat. Genet.* **23**, 319–22 (1999).

583   41.   Karamchedu, N. P. *et al.* Superficial zone cellularity is deficient in mice lacking lubricin: a

584   stereoscopic analysis. *Arthritis Res. Ther.* **18**, 64 (2016).

585   42.   Lavoie, J. *et al.* Mapping Articular Cartilage Biomechanical Properties of Normal and

586   Osteoarthritis Mice Using In. in *Osteoarthritis Cartilage 23:A524* (2015).

587   doi:10.1016/j.joca.2015.02.463.

588   43.   Korhonen, R. . *et al.* Importance of the superficial tissue layer for the indentation stiffness of

589   articular cartilage. *Med. Eng. Phys.* **24**, 99–108 (2002).

590   44.   Froimson, M. I., Ratcliffe, A., Gardner, T. R. & Mow, V. C. Differences in patellofemoral

591   joint cartilage material properties and their significance to the etiology of cartilage surface

592   fibrillation. *Osteoarthr. Cartil.* **5**, 377–386 (1997).

593   45.   Samosky, J. T. *et al.* Spatially-localized correlation of dGEMRIC-measured GAG distribution

594   and mechanical stiffness in the human tibial plateau. *J. Orthop. Res.* **23**, 93–101 (2005).

595   46.   Moshtagh, P. R., Pouran, B., Korthagen, N. M., Zadpoor, A. A. & Weinans, H. Guidelines for

596   an optimized indentation protocol for measurement of cartilage stiffness : The effects of spatial

597   variation and indentation parameters. *J. Biomech.* **49**, 3602–3607 (2016).

598   47.   Poulet, B., Westerhof, T. A. T., Hamilton, R. W., Shefelbine, S. J. & Pitsillides, A. A.

599   Spontaneous osteoarthritis in Str/ort mice is unlikely due to greater vulnerability to mechanical

600   trauma. *Osteoarthr. Cartil.* **21**, 756–763 (2013).

601   48.   Kotwal, N., Li, J., Sandy, J., Plaas, A. & Sumner, D. R. Initial application of EPIC-μCT to

602   assess mouse articular cartilage morphology and composition: Effects of aging and treadmill

603   running. *Osteoarthr. Cartil.* **20**, 887–895 (2012).

604   49.   Julkunen, P., Korhonen, R. K., Herzog, W. & Jurvelin, J. S. Uncertainties in indentation

605   testing of articular cartilage: A fibril-reinforced poroviscoelastic study. *Med. Eng. Phys.* **30**,

606   506–515 (2008).

607   50.   Simha, N. K., Jin, H., Hall, M. L., Chiravarambath, S. & Lewis, J. L. Effect of indenter size on

608   elastic modulus of cartilage measured by indentation. *J. Biomech. Eng.* **129**, 767–775 (2007).

609   51.   Drewniak, E. I. *et al.* Cyclic loading increases friction and changes cartilage surface integrity

610   in lubricin-mutant mouse knees. *Arthritis Rheum.* **64**, 465–473 (2012).

611   52.   Laasanen, M. S. *et al.* Biomechanical properties of knee articular cartilage. *Biorheology* **40**,

612   133–40 (2003).

613   53.   Rahmati, M., Nalesso, G., Mobasheri, A. & Mozafari, M. Aging and osteoarthritis: Central

614   role of the extracellular matrix. *Ageing Res. Rev.* **40**, 20–30 (2017).

615   54.   Julkunen, P. *et al.* Biomechanical, biochemical and structural correlations in immature and

616   mature rabbit articular cartilage. *Osteoarthr. Cartil.* **17**, 1628–1638 (2009).

617   55.   Mow, V. C., Kuei, S. C., Lai, W. M. & Armstrong, C. G. Biphasic creep and stress relaxation

618   of articular cartilage in compression: Theory and experiments. *J. Biomech. Eng.* **102**, 73–84

619   (1980).

620   56.   Julkunen, P., Harjula, T., Marjanen, J., Helminen, H. J. & Jurvelin, J. S. Comparison of single-

621   phase isotropic elastic and fibril-reinforced poroelastic models for indentation of rabbit

622   articular cartilage. *J. Biomech.* **42**, 652–656 (2009).

623   57.   Abubacker, S. *et al.* Absence of Proteoglycan 4 (Prg4) Leads to Increased Subchondral Bone

624   Porosity Which Can Be Mitigated Through Intra - Articular Injection of PRG4. *J. Orthop. Res.*

625   **37**, (2019).

626   58.   Jablonski, C. L., Besler, B. A., Ali, J. & Krawetz, R. J. p21−/− Mice Exhibit Spontaneous

627   Articular Cartilage Regeneration Post-Injury. *Cartilage* 1947603519876348 (2019)

628   doi:10.1177/1947603519876348.

629   59.   Richard, D. *et al.* Evolutionary Selection and Constraint on Human Knee Chondrocyte

630   Regulation Impacts Osteoarthritis Risk. *Cell* **181**, 362-381.e28 (2020).

631   60.   Hildebrand, T. & Ruegsegger, P. A new method for the model-independent assessment of

632   thickness in three-dimensional images. *J. Microsc.* **185**, 67–75 (1997).

633   61.   Lowekamp, B. C., Chen, D. T., Ibáñez, L. & Blezek, D. The design of simpleITK. *Front.*

634   *Neuroinform.* **7**, 1–14 (2013).

635   62.   Koo, T. K. & Li, M. Y. A Guideline of Selecting and Reporting Intraclass Correlation

636   Coefficients for Reliability Research. *J. Chiropr. Med.* (2015) doi:10.1016/j.jcm.2016.02.012.

637   63.   Müller, R. & Büttner, P. A critical discussion of intraclass correlation coefficients. *Stat. Med.*

638   **13**, 2465–2476 (1994).

639

640

641

29

1   **Supplementary Material**
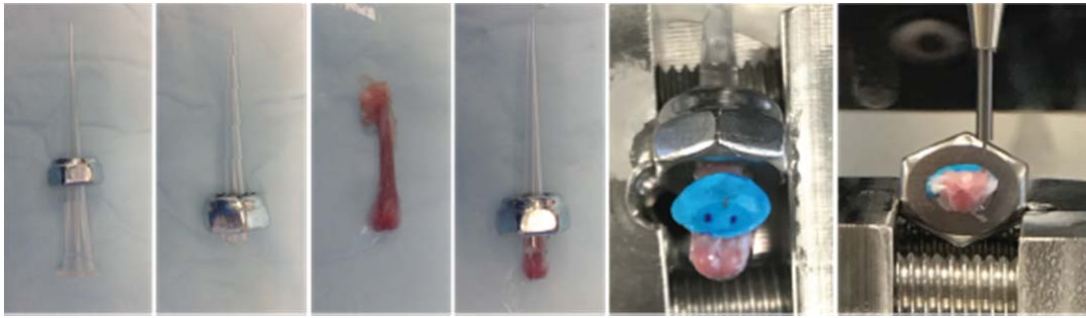
2

3   **Figure S1.** Specimen preparation and assemble to sample holder for automated indentation mapping
4   using custom setup, allowing for repositioning of the sample and non-destructive retrieval for 3D
5   XRM imaging.

6

7

8

9

10

11

12

13

14

15

16

17

18

19

20

21

22

23

24

25

26

27

28

29

Table S1. Mean peak force ($\bar{X}$: N) and coefficient of variation (CV: %) from triplicate measurements for each of the 31 positions (L1-M17) of assessment over mice femoral condyles.

		S01		S02		S03		S04		S05		S06		S07		S08		S09		S10	
	$\bar{X}$	CV	$\bar{X}$	CV	$\bar{X}$	CV	$\bar{X}$	CV	$\bar{X}$	CV	$\bar{X}$	CV	$\bar{X}$	CV	$\bar{X}$	CV	$\bar{X}$	CV	$\bar{X}$	CV
L1	0.08	2.9	0.08	3.0	0.10	4.1	0.13	1.8	0.09	12.1	0.10	2.7	0.10	4.9	0.09	3.3	0.07	1.5	0.11	0.2
L2	0.11	1.3	0.09	2.5	0.10	2.3	0.14	6.1	0.12	8.2	0.11	4.5	0.13	4.9	0.11	6.1	0.07	13.7	0.11	5.7
L3	0.07	4.9	0.08	3.6	0.08	5.0	0.12	2.5	0.11	4.8	0.12	1.5	0.09	3.8	0.08	4.9	0.07	8.5	0.08	8.0
L4	0.10	7.2	0.07	2.8	0.10	1.3	0.11	1.6	0.08	3.6	0.11	4.7	0.13	2.2	0.09	3.0	0.06	4.8	0.09	5.5
L5	0.16	0.7	0.15	5.0	0.21	9.0	0.14	7.7	0.12	7.8	0.04	10.0	0.17	2.4	0.17	4.2	0.11	6.0	0.19	6.3
L6	0.06	9.3	0.07	7.4	0.08	13.4	0.12	4.1	0.09	5.7	0.08	2.9	0.06	9.0	0.06	6.9	0.08	6.0	0.07	5.8
L7	0.06	4.7	0.07	6.2	0.08	6.9	0.10	3.1	0.07	12.3	0.07	3.8	0.09	8.0	0.08	4.9	0.07	3.8	0.07	7.5
L8	0.16	2.2	0.09	15.9	0.19	3.2	0.14	4.9	0.11	7.9	-	-	0.20	5.8	0.17	3.1	0.12	3.5	0.12	6.5
L9	0.05	10.3	0.07	5.4	0.08	2.4	0.09	1.5	0.03	20.2	0.07	0.3	0.05	6.4	0.07	2.9	0.09	0.9	0.08	2.5
L10	0.04	4.2	0.07	6.8	0.07	3.1	0.08	4.5	-	-	0.08	3.3	0.07	3.9	0.07	5.5	0.07	1.1	0.08	3.2
L11	0.10	5.7	0.08	6.1	0.15	2.4	0.11	9.1	0.13	5.1	0.14	6.8	0.16	5.9	0.14	3.7	0.04	9.0	0.11	1.3
L12	0.05	0.9	0.08	4.6	0.07	9.4	0.07	3.6	-	-	0.09	3.1	0.06	6.2	0.06	8.8	0.11	3.6	0.10	3.3
L13	0.05	3.0	0.07	3.6	0.07	6.4	0.07	5.8	-	-	0.10	2.3	0.07	2.9	0.08	4.9	0.09	0.9	0.09	6.0
L14	0.08	5.0	0.08	5.7	0.13	4.9	0.10	4.9	0.04	19.0	0.14	1.1	0.14	3.7	0.16	1.7	0.09	12.0	0.12	1.4
M1	0.29	3.7	0.18	6.9	0.23	4.1	0.23	1.9	0.21	5.5	0.26	1.4	0.22	6.7	0.20	2.2	0.20	1.7	0.22	1.9
M2	-	-	0.25	4.6	0.25	3.2	0.26	1.0	0.28	2.3	0.29	2.1	0.27	1.5	0.24	6.3	0.20	5.4	0.29	0.9
M3	0.23	3.1	0.17	3.8	0.24	0.7	0.24	1.4	0.24	2.8	0.24	1.8	0.23	3.2	0.19	2.7	0.22	6.7	0.25	3.4
M4	0.36	5.0	0.30	6.5	0.28	0.6	0.30	2.6	0.29	3.1	0.31	2.7	0.25	5.8	0.26	3.1	0.19	4.5	0.30	2.7
M5	-	-	0.38	10.0	0.30	3.9	0.30	1.9	0.36	1.1	0.26	0.7	0.30	2.4	0.25	5.5	0.18	4.3	0.15	5.1
M6	0.19	1.7	0.17	6.3	0.25	3.4	0.23	3.8	0.19	5.6	0.26	2.3	0.21	0.7	0.11	10.9	0.16	3.9	0.20	15.1
M7	0.30	3.3	0.30	4.2	0.34	5.9	0.30	1.9	0.37	7.0	0.31	1.7	0.26	2.2	0.28	1.1	0.16	1.4	0.30	6.9
M8	0.37	3.3	0.36	6.2	0.33	2.0	0.28	5.1	0.35	5.6	0.23	2.0	0.23	6.0	0.17	3.6	0.13	1.7	0.14	4.2
M9	0.20	3.8	0.16	2.5	0.27	5.6	0.21	2.8	0.18	19.6	0.25	1.2	0.20	4.2	0.16	0.9	0.15	3.4	0.24	18.6
M10	0.26	2.8	0.30	2.0	0.33	7.1	0.28	1.2	0.39	2.2	0.25	2.4	0.19	2.5	0.25	2.0	0.16	2.4	0.24	2.7
M11	0.28	2.0	0.30	2.8	0.30	6.0	0.21	1.6	0.31	3.8	0.22	2.0	0.16	1.1	0.14	0.7	0.13	7.8	0.11	7.1
M12	0.16	1.6	0.19	5.9	0.25	1.6	0.18	0.6	0.17	2.3	0.18	6.4	0.15	6.9	0.18	5.7	0.09	7.7	-	-
M13	0.22	4.3	0.26	4.6	0.29	3.0	0.20	2.3	0.32	4.0	0.20	2.6	0.15	1.2	0.21	3.6	0.14	0.1	0.20	2.9
M14	0.19	1.6	0.27	1.2	0.25	4.2	0.17	2.6	0.27	1.2	0.20	0.8	0.14	2.9	0.13	4.1	0.12	3.2	0.12	1.8
M15	0.16	3.7	0.16	0.5	0.18	1.6	0.14	1.6	0.18	0.7	0.13	1.9	0.13	1.7	0.14	1.1	0.14	1.6	0.21	9.2
M16	0.14	1.3	0.19	1.3	0.20	0.9	0.14	2.1	0.22	1.4	0.16	2.7	0.12	0.8	0.15	1.2	0.13	1.4	0.16	1.7
M17	0.14	2.2	0.21	1.1	0.17	3.4	0.15	2.6	0.19	3.1	0.15	5.5	0.13	2.1	0.12	3.0	0.13	1.4	0.13	2.2

3

1
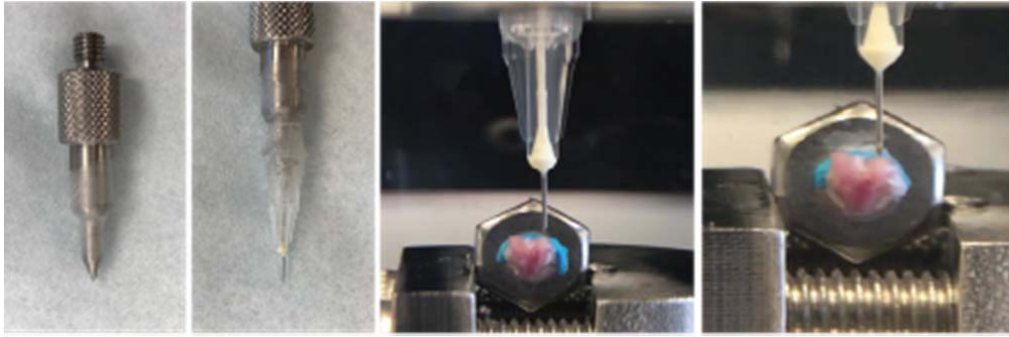
2

3 **Figure S2.** Setup for needle probing thickness measurement, using a 30G x 1.4" hypodermic needle
4 (TSK Laboratory, Japan) adapted to the 1 mm spherical indenter (*Biomomentum Inc.*, Laval, QC).

5

6

7

8

1 **Table S2.** Mean and standard deviation (SD) values for cartilage thickness as determined by XRM
2 imaging for distal femur samples of murine articular cartilage ($n = 10$). Mean values compared between
3 condyles (Lateral/Medial; unpaired, Student's t test) and within sub-regions of condyles (Lat/Ant,
4 Lat/Post, Med/Ant, Med/Post; *one-way* ANOVA). *p*-value reported.
5

Cartilage Thickness [N]				
Condyle	Mean (SD)	Condyle	Mean (SD)	Lat - Med
Lateral	64.4 (8.4)	Medial	46.5 (4.4)	*p* < 0.0001
Lat/Ant	59.0 (8.2)	*Med/Ant*	42.9 (5.1)	*p* < 0.0001
Lat/Post	67.4 (9.7)	*Med/Post*	49.5 (4.3)	*p* < 0.0001
Ant - Post	*ns*	Ant - Post	*ns*	-

6 *ns,* no significant difference; -, comparison not applicable

7